Nanoscale Advances

ROYAL SOCIETY OF CHEMISTRY

PAPER

View Article Online
View Journal | View Issue

Cite this: *Nanoscale Adv.*, 2021, **3**, 3145

Pillared Mo_2TiC_2 MXene for high-power and long-life lithium and sodium-ion batteries†

Philip A. Maughan,[a] Luc Bouscarrat,[a] Valerie R. Seymour,[b] Shouqi Shao,[c] Sarah J. Haigh,[c] Richard Dawson,[a] Nuria Tapia-Ruiz *[b] and Nuno Bimbo ‡*[a]

In this work, we apply an amine-assisted silica pillaring method to create the first example of a porous Mo_2TiC_2 MXene with nanoengineered interlayer distances. The pillared Mo_2TiC_2 has a surface area of 202 m^2 g^{-1}, which is among the highest reported for any MXene, and has a variable gallery height between 0.7 and 3 nm. The expanded interlayer distance leads to significantly enhanced cycling performance for Li-ion storage, with superior capacity, rate capably and cycling stability in comparison to the non-pillared analogue. The pillared Mo_2TiC_2 achieved a capacity over 1.7 times greater than multilayered MXene at 20 mA g^{-1} (≈320 mA h g^{-1}) and 2.5 times higher at 1 A g^{-1} (≈150 mA h g^{-1}). The fast-charging properties of pillared Mo_2TiC_2 are further demonstrated by outstanding stability even at 1 A g^{-1} (under 8 min charge time), retaining 80% of the initial capacity after 500 cycles. Furthermore, we use a combination of spectroscopic techniques (*i.e.* XPS, NMR and Raman) to show unambiguously that the charge storage mechanism of this MXene occurs by a conversion reaction through the formation of Li_2O. This reaction increases by 2-fold the capacity beyond intercalation, and therefore, its understanding is crucial for further development of this family of materials. In addition, we also investigate for the first time the sodium storage properties of the pillared and non-pillared Mo_2TiC_2.

Received 1st February 2021
Accepted 11th April 2021

DOI: 10.1039/d1na00081k

rsc.li/nanoscale-advances

Introduction

Over recent years, there has been incredible growth in the research and application of Li-ion batteries (LIBs), which are now widely used in portable electronics, electric vehicles and grid storage applications.[1,2] However, further uptake of these technologies in more demanding applications, such as fast-charging electric vehicles and grid storage, requires significant improvements in high-rate charging and cycling lifetime, without compromising their energy density. Since these characteristics are determined by the electrode materials, there is an urgent need to develop new materials that can satisfy these demands. The negative electrodes that are currently used for Li-ion batteries often suffer from poor rate capability (for example, the state-of-the-art negative electrode material graphite), and those with an impressive performance at high rates cannot achieve high capacities overall (lithium titanate only achieves capacities around 150 mA h g^{-1} and niobium oxides have a capacity of 200 mA h g^{-1}.[3–5]

Two-dimensional (2D) materials such as graphene have emerged as promising candidates for next-generation high-rate negative electrode materials due to their combination of high electrical conductivity and large 2D channels, which allow for fast electron and Li^+ diffusion, respectively, facilitating fast charging times.[6] However, 2D materials typically suffer from issues such as restacking of nanosheets during cycling, which can block Li diffusion channels, leading to lowered capacities, rate capabilities and cycling stabilities.[7] It is therefore crucial to develop methods which give rise to controlled open electrode architectures that are stable even when cycled at high rates.

MXenes are an exciting family of 2D materials which have attracted significant research attention since their discovery in 2011, especially in the field of energy storage.[8–11] They have demonstrated multiple advantageous properties for LIBs such as higher conductivity and large tuneable interlayer spacings. These enable excellent rate capability and cycling stability compared to practical liquid-processed films from other 2D materials such as transition metal dichalcogenides (TMD) and reduced graphene oxides (rGO).[12–14] In addition, MXenes typically have much higher tap density than TMDs and graphenes, which would result in significantly higher volumetric energy density in batteries.[14] However, like other 2D materials, electrode architecture plays a crucial role in their electrochemical performance, with multilayered or restacked MXenes showing

[a]*Department of Engineering, Lancaster University, Lancaster, LA1 4YW, UK. E-mail: n.bimbo@soton.ac.uk*

[b]*Department of Chemistry, Lancaster University, Lancaster, LA1 4YB, UK. E-mail: n.tapiaruiz@lancaster.ac.uk*

[c]*Department of Materials, University of Manchester, Manchester, M13 9PL, UK*

† Electronic supplementary information (ESI) available. See DOI: 10.1039/d1na00081k

‡ Current address: School of Chemistry, University of Southampton, Southampton, SO17 1BJ, UK.

poor cycling performance.[15,16] Titanium-based MXenes such as Ti_2C or Ti_3C_2 dominate research in this area, despite more than 30 different MXenes having been synthesised to-date.[17] This is particularly important because Ti-based MXenes suffer from poor initial coulombic efficiencies (typically 40–60%), which severely limit their application in full cells.[18] In 2015, Anasori *et al.* first reported Mo_2TiC_2, an out-of-plane ordered MXene, with Mo occupying the outer metal layers, while the inner metal layer is exclusively Ti.[19] This allows the effect of the outer metal element to be studied, since Mo_2TiC_2 is otherwise analogous to Ti_3C_2.[19] Despite this, there have only been a handful of reports on this MXene,[19–23] with only one other reporting LIB performance.[21] Mo_2TiC_2 had several promising features for LIB applications, with delaminated Mo_2TiC_2 showing capacities up to 260 mA h g^{-1}, an initial coulombic efficiency of 86% and low average voltage.[19]

Unlike Ti-based MXenes, the load curve for Mo_2TiC_2 displayed a plateau below 0.6 V, suggesting a different charge storage mechanism compared to MXenes without Mo. Computational studies implied that a conversion reaction occurs between lithiated Mo–O surface groups (formed *via* Li intercalation in reaction (1) and two further moles of Li, as shown by reaction (2)), boosting the capacity.[19] The theoretical capacity achieved in reaction (1) is 180 mA h g^{-1}, which increases to 356 mA h g^{-1} after the proposed conversion reaction.

$$Mo_2TiC_2O_2 + 2Li^+ + 2e^- \rightarrow Mo_2TiC_2O_2Li_2 \quad (1)$$

$$Mo_2TiC_2O_2Li_2 + 2Li^+ + 2e^- \rightarrow Mo_2TiC_2 + 2Li_2O \quad (2)$$

The proposed mechanism is similar to the lithiation of Mo oxides, which is accompanied by large volume changes, causing significant capacity fade.[24] This could explain the relatively high fade seen in previous Mo_2TiC_2 studies,[19,21] demonstrating the need to develop methods that optimise the electrode architecture and increase the cycling stability of this material. There have been no reports to-date on engineered electrode architectures for Mo_2TiC_2 in electrochemical applications, despite the clear promise of this material. Furthermore, previous work has not experimentally verified the lithiation mechanism.

Pillaring is a technique used to make porous layered materials from non-porous precursors, by inserting foreign species into the interlayer, which expands the pore space and creates stable architectures which prevent sheets from restacking.[25] This technique has recently been applied to MXenes, and has been shown to improve performance in a variety of electrochemical energy storage applications such as Li, Na and Zn-ion batteries, aqueous supercapacitors and solid-state supercapacitors.[26–33] However, these reports have been limited to titanium-based MXenes, with no studies of pillaring having considered the wider MXene family.

In this work, we developed a porous Mo_2TiC_2 architecture using an amine-assisted pillaring technique (Fig. 1) and obtained the largest BET surface area reported for any Mo-based MXene to-date. We tested the resulting pillared Mo_2TiC_2 for electrochemical Li- and Na-ion storage, and obtained significantly enhanced performance, with superior capacities, rate capabilities and cycling stabilities compared to the non-pillared version, proving the effectivity of this pillaring method. Furthermore, the charge compensation mechanism in Mo-based MXenes was investigated for the first time, using a combination of spectroscopic techniques, including nuclear magnetic resonance spectroscopy (NMR), X-ray photoelectron spectroscopy (XPS) and Raman spectroscopy. We believe that these fundamental studies are crucial for the future development of this class of MXene materials as electrodes in LIBs in order to achieve high-rates and long cycle-life. In addition, due to the growing importance of Na-ion battery research as a promising low-cost alternative to LIBs, we also report for the first time results for the use of Mo_2TiC_2 in Na-ion half-cells.

Results

MAX phase and MXene synthesis

The Mo_2TiAlC_2 MAX phase was synthesised following previously reported methods, with details given in the experimental section.[19,34] The powder X-ray diffraction (PXRD) data matches previous reports, showing the successful synthesis of Mo_2TiAlC_2 (Fig. 2a).[19]

To avoid the risk associated with handling HF, the synthesis of Mo_2TiC_2 was carried out for the first time using an adapted version of the LiF–HCl method which has been successfully used for titanium-based MXenes.[35] Details of this can be found in the experimental section. PXRD data are in agreement with previously reported X-ray diffraction data for Mo_2TiC_2,[19] demonstrating that the Mo_2TiC_2 MXene was successfully etched using the described method (Fig. 2a). The (002) diffraction peak of Mo_2TiC_2 has shifted to a lower angle compared to the MAX phase (to *ca.* 7° 2θ), and has increased in intensity, as expected for the formation of a MXene phase.[36] Both the (002) and (004) diffraction peaks have shifted to higher angles, implying a larger *d*-spacing compared to previously reported HF-etched Mo_2TiC_2,[19] which is consistent with the pre-intercalation of Li during the etching method, as has been observed for Ti_3C_2.[35] A small peak at 9.5° 2θ, which corresponds to the (002) diffraction peak of Mo_2TiAlC_2, indicates that a minimal impurity corresponding to the original MAX phase remains. High-angle annular dark-field scanning transmission electron microscopy (HAADF-STEM) and energy dispersive X-ray spectroscopy (EDS) were also carried out to further confirm the formation of the Mo_2TiC_2 MXene. HAADF-STEM micrographs (Fig. 2b and c) show the layered morphology typical of an MXene in the etched material, with an interlayer spacing *ca.* 1.2 nm, supporting the PXRD results. Scanning electron microscopy (SEM) revealed the flakes have lateral dimensions in the range of 1–10 μm (Fig. S1†), with thicknesses between 1 and 5 μm, which are similar in size to other reported MXenes, including Mo_2TiC_2.[19] SEM-EDS and STEM-EDS analysis show that the MXene consist of homogenously distributed Mo, Ti and C (Fig. 2c–f), with quantification revealing an atomic ratio of approximately 1 : 0.5 : 1 (normalised to Mo), which supports the expected stoichiometry (Fig. S1 and S2†). SEM-EDS confirmed that the flakes contain no Al, demonstrating successful etching of the

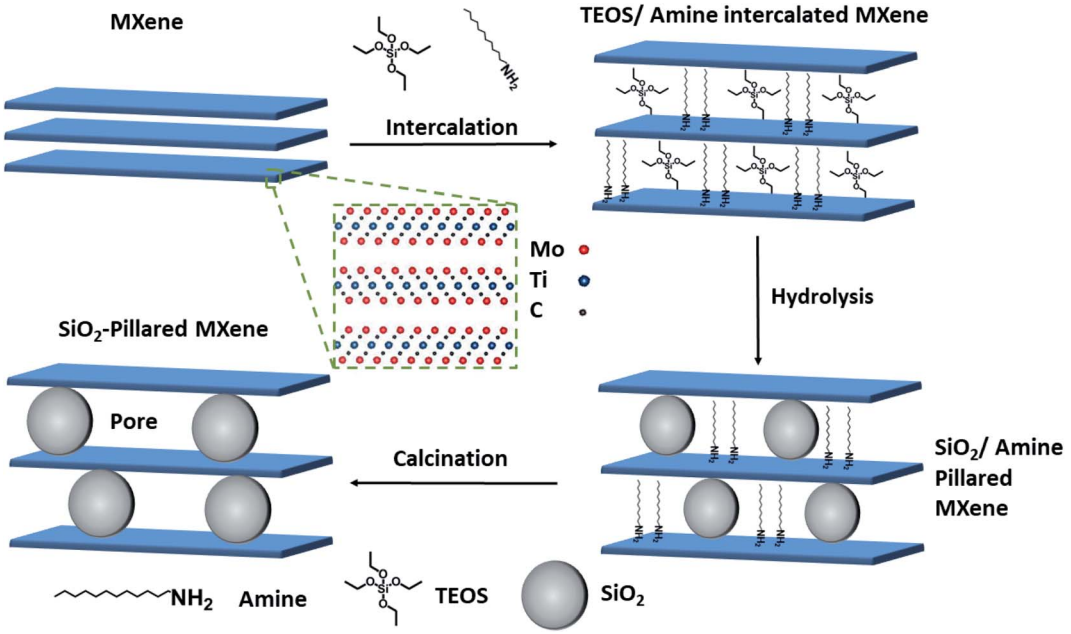

Fig. 1 Schematic representation of the amine-assisted silica pillaring method. Inset (dashed green box) illustrates the crystal structure of the out–out-plane ordered Mo_2TiC_2 MXene before pillaring. Intercalation with dodecylamine (DDA) and tetraethyl orthosilicate (TEOS) is used to form Mo_2TiC_2–Si, followed by hydrolysis and calcination steps to form the pillared material, Mo_2TiC_2–Si-400.

MAX phase and that Mo_2TiC_2 is terminated with –O and/or –OH groups (21 at%) and –F groups (3 at%), akin to its Ti_3C_2 counterpart (Fig. S1†). BET analysis (Fig. 2h) using a nitrogen isotherm at 77 K showed the as-made MXene was non-porous, with a low specific surface area of 8 $m^2\ g^{-1}$.

Having confirmed the successful synthesis of the Mo_2TiC_2, we then applied our previously reported amine-assisted SiO_2 pillaring method to this MXene (see Fig. 1 and the Experimental section).[37] Throughout the paper, we refer to the pillared sample intercalated with dodecylamine (DDA) and tetraethyl orthosilicate (TEOS) as Mo_2TiC_2–Si and the pillared sample after calcination at 400 °C as Mo_2TiC_2–Si-400.

PXRD data show a clear shift in the (002) diffraction peak of Mo_2TiC_2–Si from 7 to 2.5° 2θ, demonstrating intercalation (Fig. 2g). This gives an increased *d*-spacing of *ca.* 3.6 nm, corresponding to a gallery height of around 2.6 nm, larger than any reported for other layered Mo-based materials such as Mo_2C and MoS_2 (Table S1†).[22,38–40] After calcination (Mo_2TiC_2–Si-400), the (002) diffraction peak shifts to a higher angle of 4.5° 2θ (Fig. 2g), corresponding to a *d*-spacing of around 2 nm, which gives a gallery height of 1 nm. The shift suggests that the DDA template is successfully removed, which is also supported by the loss of peaks corresponding to DDA in the Raman spectra for this material (Fig. S3†). SEM and STEM studies (Fig. 3a–c) also confirm that the layered morphology of the MXene is retained after calcination, albeit with slightly lower interlayer distances measured compared to the PXRD results (2.04 ± 0.26 nm after intercalation, and 1.50 ± 0.41 nm after calcination from STEM measurements). We have seen such discrepancies between PXRD and STEM data in our previous works.[37] STEM-EDS results demonstrate significant Si content (*ca.* 2.6 at%) in the final material (Fig. S2†). The Si does not form clusters across the MXene flake, and surface crystals of SiO_2 are not visible. This supports the formation of nanoscale SiO_2 pillars between the MXene layers, since Si is shown to be distributed evenly across the flake. Prior to calcination, STEM-EDS mapping (Fig. S4†) showed significant increases in Si concentration at the edges of the flakes, suggesting the initial Si intercalation favours near surface sites in the MXene. The calcination step then allows a deeper intercalation of the Si, increasing homogeneity of the Si distribution, demonstrating the importance of the calcination stage to create a well pillared porous product.

BET analysis revealed that the pillaring procedure resulted in a substantial increase in BET specific surface area, with the pillared Mo_2TiC_2 MXene (Mo_2TiC_2–Si-400) obtaining a surface area of 202 $m^2\ g^{-1}$ compared to around 8 $m^2\ g^{-1}$ for the non-pillared material (Fig. 2h). This is one of the largest surface areas reported for any MXene, and the largest for a non-Ti based MXene.[15,41–44] Additionally, this is also larger than previously reported results for pillared MoS_2 (Table S1†).[40,45] Pore size distribution analysis on the pillared MXene demonstrated the existence of pores just over 1 nm in size (Fig. S5†), in close agreement with the PXRD data (Fig. 2d), supporting the presence of large interlayer pores in the pillared MXene. For the remainder of the manuscript, pillared Mo_2TiC_2 refers to the calcined material Mo_2TiC_2–Si-400.

To further investigate the structure of the synthesised Mo_2TiC_2 and the effect of the pillaring process on the MXene, X-ray photoelectron spectroscopy (XPS) was used to study the Mo, Ti and O valence states and surface functional groups in the as-made and pillared MXene, and Si was also studied in the pillared material (Mo_2TiC_2–Si-400). We note that high resolution

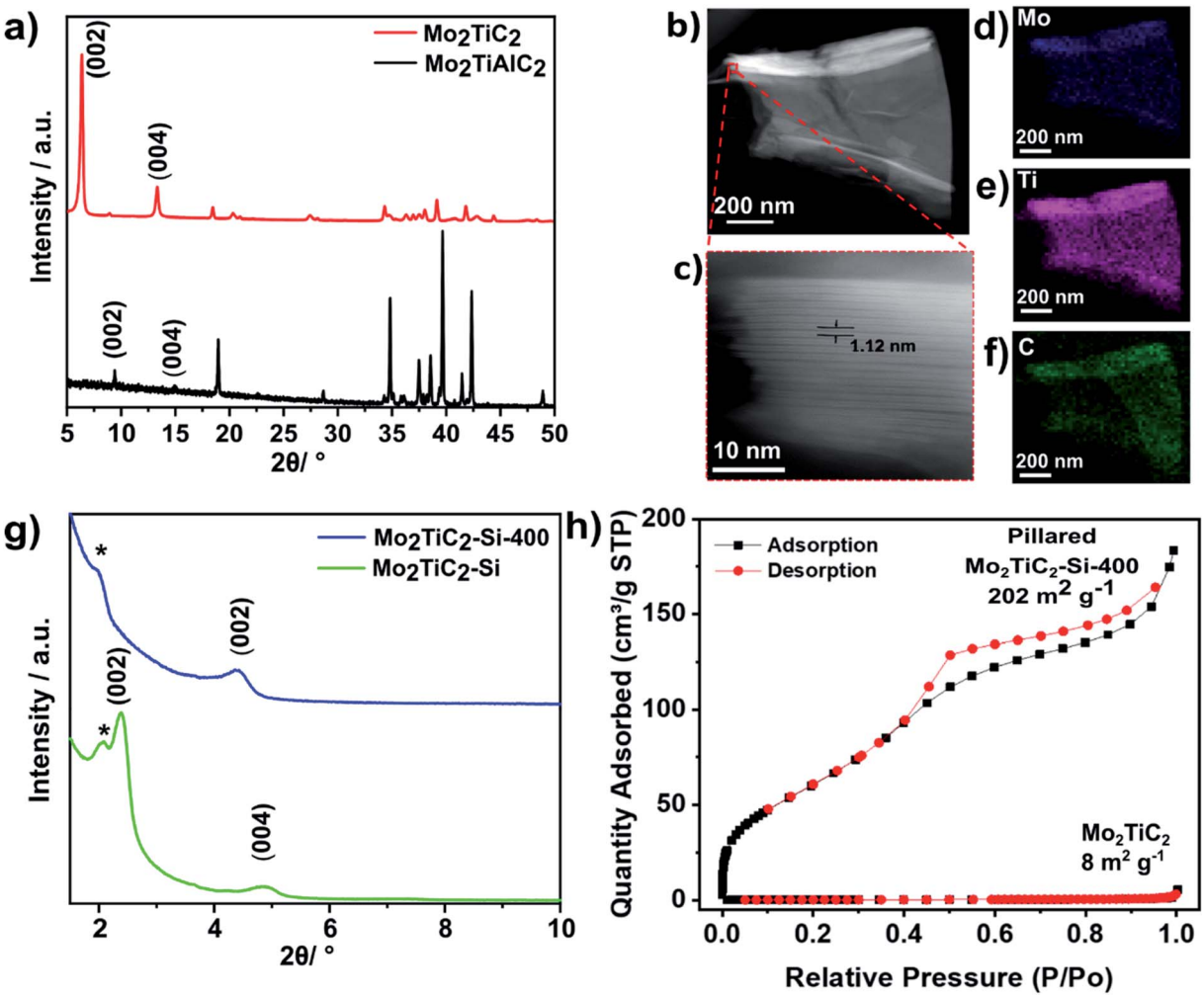

Fig. 2 (a) PXRD data of the as-synthesised Mo_2TiAlC_2 MAX phase (bottom) and Mo_2TiC_2 MXene (top). (b) HAADF-STEM micrograph of Mo_2TiC_2. The dashed red square highlights the region shown in the expansion in (b). (c) Expanded HAADF-STEM micrograph of the highlighted area in (b). (d–f) STEM-EDS maps of (b). (g) Low angle PXRD data of the intercalated (Mo_2TiC_2–Si) and calcined (Mo_2TiC_2–Si-400) pillared MXene materials. (*) denotes a peak from the glass sample holder. (h) N_2 adsorption–desorption curves at 77 K for the pillared (Mo_2TiC_2–Si-400) and non-pillared Mo_2TiC_2.

XPS is capable is distinguishing between multiple similar species commonly found within MXenes, such surface –O and –OH groups, and intercalated water, and is therefore more powerful than alternative techniques such as infra-red (IR) spectroscopy.[20,46] Fig. 4 shows the Mo 3d XPS spectra for the non-pillared and pillared Mo_2TiC_2. There are three main peaks visible in both samples centred at 229.8, 233.0 and 236.0 eV for Mo_2TiC_2 and 229.7, 232.9 and 236.1 eV for Mo_2TiC_2–Si-400. These peaks are in good agreement with a previous report on Mo_2TiC_2 Mo 3d XPS spectra, supporting a successful Mo_2TiC_2 synthesis.[20] It is known that the large peaks at around 229.8 and 233.0 eV correspond to the electrons in the $3d_{5/2}$ and $3d_{3/2}$ levels for the expected MXene Mo environment (Mo–C), which indicates that 4^+ is the dominant oxidation state. The small peak at 236.0 eV corresponds to surface Mo oxides, (Mo^{6+}, $3d_{3/2}$ electrons) showing that, like titanium-based MXenes, Mo_2TiC_2 also undergoes a slight surface oxidation either during the etching process or when exposed to ambient conditions.[47] The Mo^{6+} $3d_{5/2}$ electrons contribute to the peak centred around 233.0 eV, with an expected binding energy of 232.7 eV. The presence of a small amount of these surface oxides has also been reported previously for Mo_2TiC_2, where HF etching was used.[48] The surface oxide peaks do not appear to grow after pillaring and calcination, suggesting that the Ar atmosphere during calcination was sufficient to avoid further oxidation of the MXene. Ti 3d XPS spectra (Fig. 4c and S5†) follows the same pattern, with 3^+ being the dominant oxidation state and some Ti^{4+} oxides also present.

XPS results for the O 1s scans show clear differences between the non-pillared and pillared Mo_2TiC_2 (Fig. 4d and e, respectively). The spectrum for the non-pillared Mo_2TiC_2 matches previous reports for this MXene and shows a very broad asymmetric peak which is comprised of a variety of components as a result of multiple oxygen-containing species being present in the sample.[20] Peak deconvolution reveals a component centred around 530.5 eV, which corresponds to the formation of Mo and

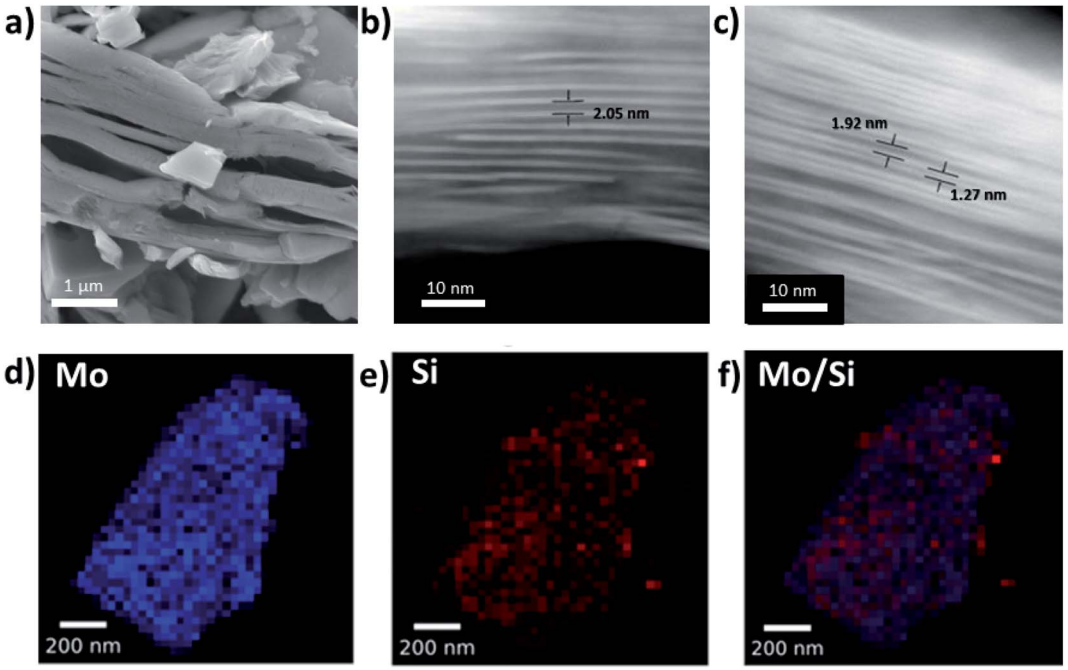

Fig. 3 (a) SEM micrograph of Mo_2TiC_2–Si-400 MXene after calcination at 400 °C for 5 h under flowing argon. (b and c) HAADF-STEM micrographs of (b) Si intercalated MXene, Mo_2TiC_2–Si, and (c) Si-pillared and calcined MXene, Mo_2TiC_2–Si-400. (d and f) STEM-EDS maps of Si-pillared MXene, Mo_2TiC_2–Si-400 showing the Mo (d) and Si (e) distribution in the pillared MXene, with the overlay shown in (f).

Ti oxides, supporting the Mo 3d and Ti 2p spectra.[20] The peak at 531.0 eV corresponds to Mo–O groups, while the peak around 532.0 eV reveals the presence of Mo–OH termination groups.[20] At 534.0 eV there is a small component which corresponds to surface-bound H_2O molecules.[20] After pillaring and calcination, there is a significant new broad peak centred around 533.2 eV,

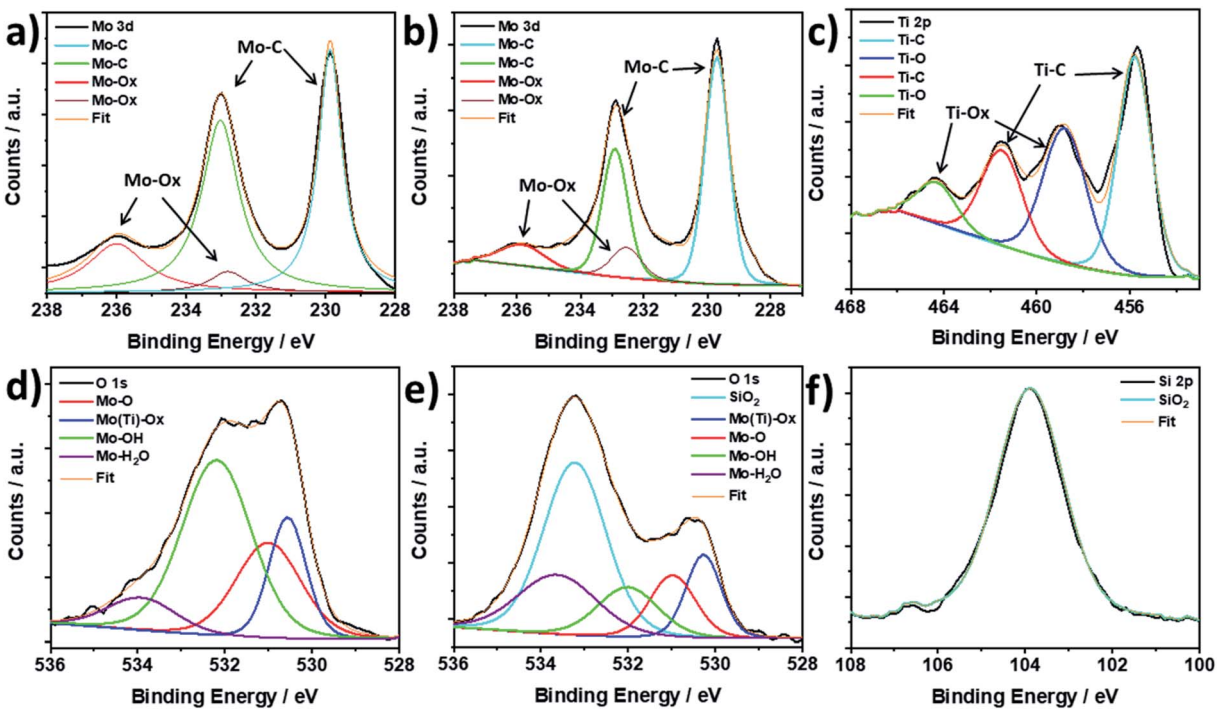

Fig. 4 Mo 3d XPS spectra for (a) non-pillared Mo_2TiC_2 and (b) Mo_2TiC_2–Si-400 after calcination at 400 °C, Mo_2TiC_2–Si-400. (c) Ti 2p XPS spectra of Mo_2TiC_2–Si-400. (d) O 1s spectra of non-pillared Mo_2TiC_2. (e) O 1s spectra of the pillared MXene Mo_2TiC_2–Si-400. (f) Si 2p spectra of the pillared MXene Mo_2TiC_2–Si-400.

which is a result of oxygen in the silica pillars.[49] There is a substantial decrease in the component relating to –OH surface groups. Before pillaring, the OH : O ratio is approximately 2 : 1, as can be seen in 4d, but decreases significantly to 1 : 1 after pillaring (4e), demonstrating the direct involvement of the –OH groups in the pillaring process, as we have reported in our previous work for Ti_3C_2.[37] Finally, the Si 2p XPS spectra for Mo_2TiC_2–Si-400 (Fig. 4f) shows a broad peak at 103.9 eV, which is consistent with SiO_2 being the pillar.[49]

Overall, these results imply that the amine-assisted pillaring method is unaffected by the change in metal in the surface layer of the MXene, and is directly applicable to Mo-based MXenes. This suggests that the pillaring method can be applied to other types of MXenes, so long as –OH surface groups are present.

Electrochemical testing in a Li-ion battery

To evaluate the electrochemical performance of the pillared structure, the Mo_2TiC_2 materials were tested in half-cells against Li metal, which acts as a counter and reference electrode. Fig. 5 shows galvanostatic cycling data in a voltage window of 0.01–3 V *vs.* Li^+/Li at a rate of 20 mA g^{-1}. The first cycle capacities for the pillared MXene are 473 and 314 mA h g^{-1} on the discharge and charge respectively (Fig. 5b), which are larger than for the non-pillared MXene (344 and 219 mA h g^{-1} respectively, Fig. 5a), and previously reported Mo_2TiC_2 (Table S2†).[19,21] The low coulombic efficiency of *ca.* 66% in the first cycle (Fig. 5) is commonly observed in MXenes and is attributed to SEI formation and irreversible reactions between surface groups and Li^+ ions.[13,50] This is lower than a previous report for Mo_2TiC_2 (86%),[19] which is likely explained by higher levels of SEI formation in the pillared MXene as a result of the significantly larger surface area, which cancels out any improvements obtained by reducing ion trapping by the removal of narrow interlayer sites. Differences in surface chemistry between the materials may also explain the variation. The coulombic efficiency in the second cycle is 94% and reaches *ca.* 99% after 18 cycles in both MXenes. Around 80% capacity is retained between the 2nd (316 mA h g^{-1}) and 94th (250 mA h g^{-1}) cycles in the pillared MXene (Fig. 5d) compared to just 54% capacity retention under the same conditions for the as-made Mo_2TiC_2. Chen *et al.* reported a capacity of only 52 mA h g^{-1} by the 100th cycle in their tests on Mo_2TiC_2,[4] which further demonstrates the remarkable improvement in cycling stability afforded by the pillaring technique reported here.

Rate capability tests were carried out at increasing rates of 20, 50, 200, 500, and 1000 mA g^{-1} with five discharge–charge cycles at each rate (Fig. 5c). The pillared material shows superior performance at all rates, delivering discharge capacities of 312, 281, 229, 182 and 143 mA h g^{-1}, respectively. When the current was returned to 20 mA g^{-1}, the capacity was recovered to 292 mA h g^{-1}. In comparison, the non-pillared Mo_2TiC_2 material delivered capacities of 205, 162, 108, 79 and 59 mA h g^{-1} at the respective rates, with 172 mA h g^{-1} recovered at 20 mA g^{-1}. Notably, the enhancement in capacity between the pillared and non-pillared MXene increases with rate, with the pillared MXene delivering capacities around 1.7 times greater than for the non-pillared MXene at 20 mA g^{-1}, and around 2.5 times greater than for the non-pillared MXene at 1 A g^{-1}. This demonstrates that the increased interlayer spacing afforded by the pillaring enables fast Li-ion transport, resulting in superior capacities at higher rates.

Since the pillared MXene showed impressive capacity at high rates, its high-rate cycling stability was then tested by continuous galvanostatic cycling at 1000 mA g^{-1} (corresponding to a charging/discharging time of 8 min) after the rate capability test. After 500 cycles at 1000 mA g^{-1}, it retained a capacity of 108 mA h g^{-1}, a capacity retention of 80% compared to the 1st cycle (135 mA h g^{-1}), (Fig. 5e). The average coulombic efficiency over these cycles was close to 100%, indicating highly reversible charge storage at this rate. This shows that Mo_2TiC_2–Si-400 is a very stable electrode, making it highly suitable for high-power and long-life batteries. In addition, a comprehensive comparison of our work with other Mo-based MXenes for LIB applications demonstrates the superior performance of our pillared Mo_2TiC_2 material (Fig. 5f and Table S2†).

The load curves for both materials, (*i.e.* non-pillared and pillared, Fig. 5a and b, respectively) display very similar features and are markedly different from titanium-based MXenes, which typically display very linear profiles.[52] In both materials the load curves show two clear regions on discharge after the first cycle, the first of which is between 3 and 0.6 V, which slopes with a linear profile and a second region between 0.6 and 0.01 V where there is a sloping plateau feature appearing, demonstrating that a different charge storage mechanism operates in this region. Closer inspection of the load curves reveals that the majority of the capacity is stored in the region below 0.6 V (215 mA h g^{-1} for the pillared material on the 2nd cycle), but that the capacity fade also occurs mostly in that region (160 mA h g^{-1}, 73%, is retained after 94 cycles for the pillared material, Mo_2TiC_2–Si-400). This capacity loss is even more dramatic in the non-pillared MXene, where the sloping plateau feature is substantially reduced during cycling to just 90 mA h g^{-1} after 94 cycles (53% capacity retention). Furthermore, differential $dQ\ dV^{-1}$ plots of both non-pillared and pillared samples (Fig. S7 and S8†) show a peak at 0.6 V, which rapidly decreases with cycling, confirming that this low voltage process contributes significantly to the capacity during the initial cycles but it is a significant cause of capacity fade over prolonged cycling.

Anasori *et al.* used density functional theory (DFT) to predict that the 0.6 V feature present in the load curves of Mo_2TiC_2 could result from a conversion reaction between Mo–O groups on lithiated $Mo_2TiC_2O_x$ (formed by Li intercalation between 3 and 0.6 V) and extra Li moles to form Li_2O.[19] Li_2O is known to be a poor electrical conductor, and it is possible that its formation, which in transition metal oxide electrodes is often poorly reversible and accompanied by a large volume change, is the main cause of the capacity fade seen in these electrodes, with several bulk oxides reporting capacity retention values between 40–50% over 100 cycles.[53] In these reports on Mo oxides, Li_2O typically forms amorphous nanosized particles which cannot be observed using techniques which rely on long-range order such as XRD.[54–56] Therefore, we used a series of spectroscopic studies

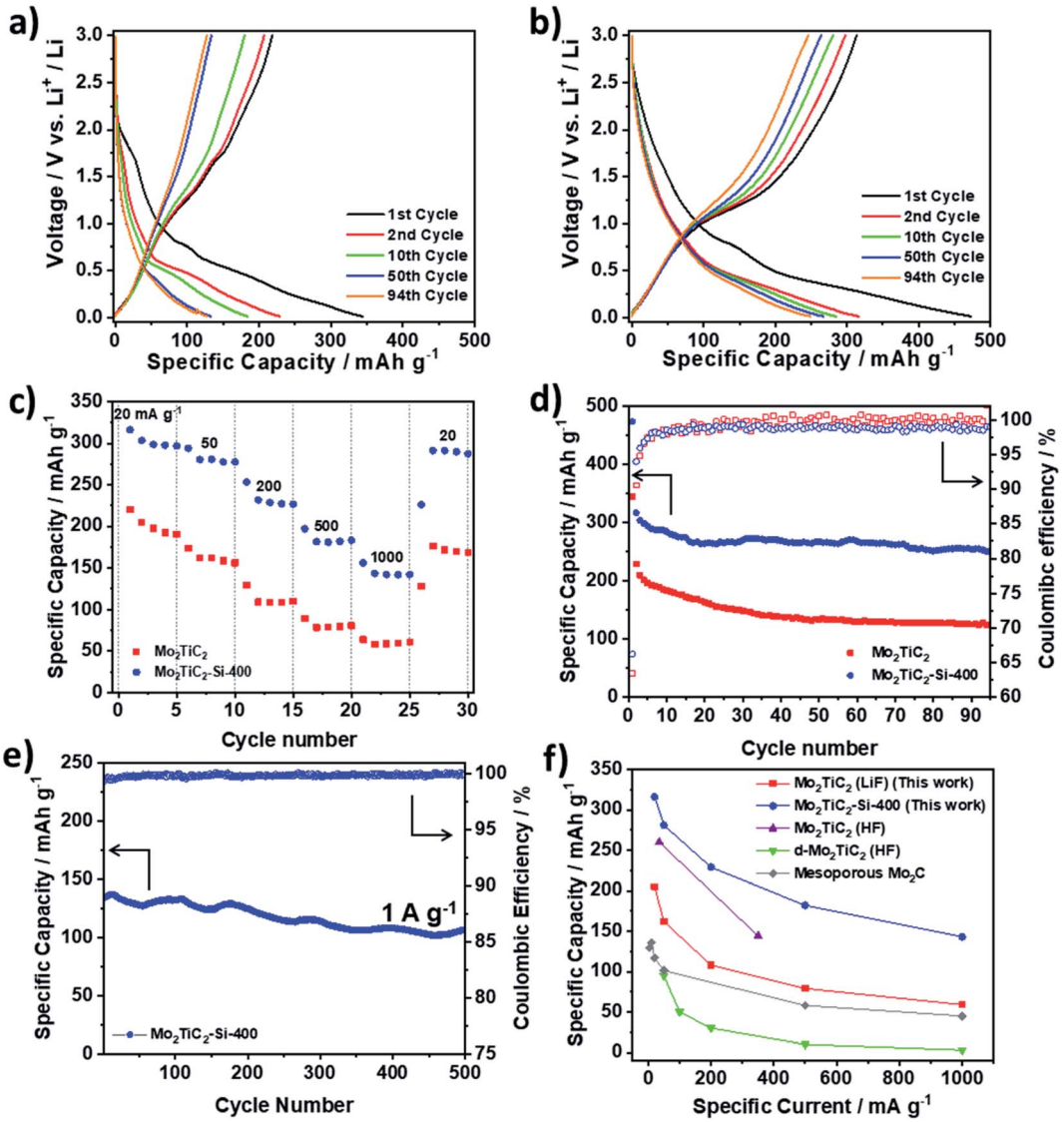

Fig. 5 Galvanostatic charge–discharge testing of Mo_2TiC_2 samples in Li-ion half-cells in a voltage range of 0.01–3 V *vs.* Li^+/Li. (a) Load curves for selected cycles of Mo_2TiC_2. (b) Load curves for selected cycles of Mo_2TiC_2–Si-400. (c) Rate capability testing at 20, 50, 200, 500, 1000 mA g^{-1} for five cycles at each rate for the pillared (blue) and non-pillared (red) samples. (d) Cycling stability data and coulombic efficiencies over 94 cycles for the pillared (blue) and non-pillared (red) samples. (e) Long-term high-rate cycling stability of Mo_2TiC_2–Si-400 at 1 A g^{-1} over 500 cycles. (f) Rate capability comparison of the performance of the Mo_2TiC_2 MXenes reported in this work with existing reports of Mo-based MXenes electrodes supported on Cu current collectors for lithium-ion batteries: Mo_2TiC_2 (HF),[19] d-Mo_2TiC_2 (HF)[21] and mesoporous Mo_2C.[51]

(NMR, XPS and Raman) to experimentally validate the charge storage mechanism for the first time. These techniques are able to probe the local structure and surface environments of materials, and are typically utilised to investigate the formation of Li_2O as a discharge product in Mo oxides.[54,55] To ensure samples were not degraded by exposure to air, all electrodes were extracted at the desired state-of-charge in an argon or nitrogen filled glovebox, washed with dimethylcarbonate (DMC) to remove any SEI components and electrolyte salts and sealed in air tight containers for transport/measurement.

To study the reactivity of the SiO_2 pillars, we combined ^{29}Si NMR and Si 2p XPS data to investigate any potential lithiation of the pillars, both in the bulk and near the surface of the pillared MXene. ^{29}Si solid-state NMR (Fig. 6c) revealed that there is only one Si environment present within the pristine pillared MXene structure, which matches well with the expected chemical shift for SiO_2 (*i.e.* −108 ppm).[57] There is no change in the ^{29}Si NMR environment after discharge or subsequent charge, confirming that the SiO_2 pillars are stable during cycling, and that no alloying reaction occurs. This is supported by *ex situ* Si 2p XPS (Fig. 6d), which also shows no significant changes in the spectra at different states-of-charge, suggesting no difference in redox activity between bulk and near-surface pillars. Additionally, no signal corresponding to Li_xSi_y alloys (expected between 20 and 10 ppm) could be distinguished in the ^7Li NMR spectra (Fig. S9†).[57,58] Significantly, this means that the improved

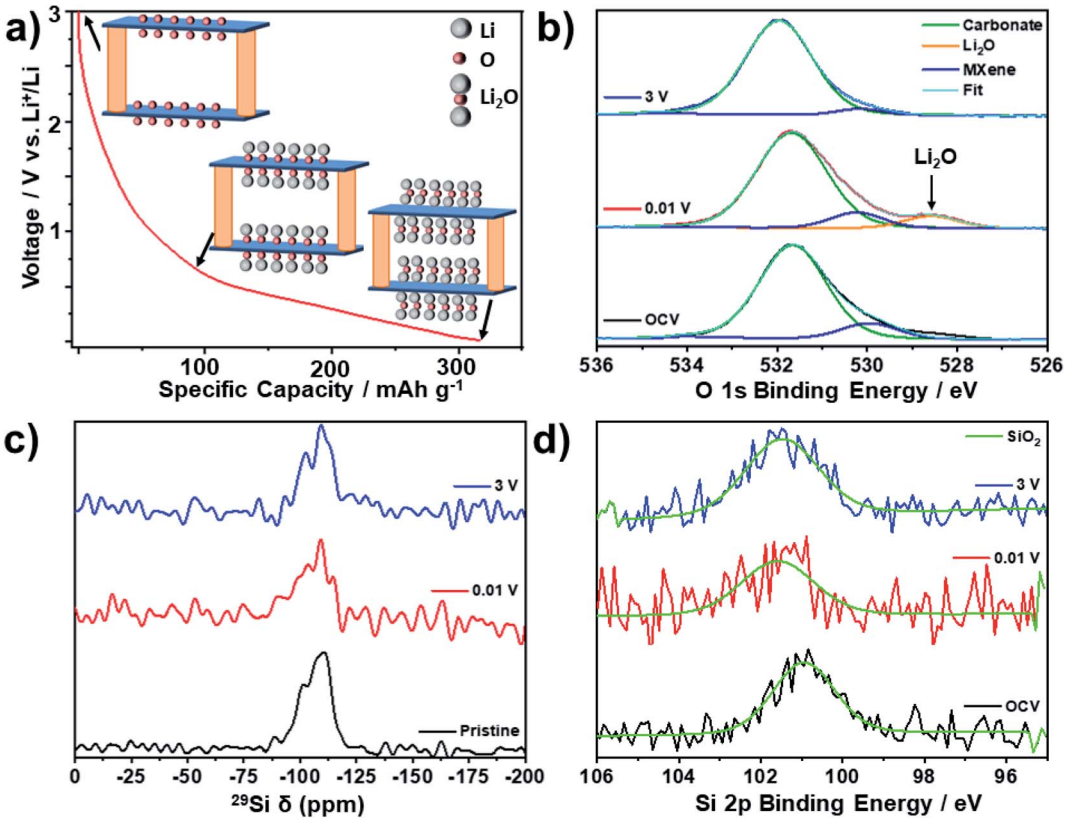

Fig. 6 *Ex situ* MAS SS-NMR spectra (16.4 T, 30 kHz MAS) and XPS spectra of Mo_2TiC_2–Si-400 at selected states-of-charge. (a) Schematic illustrating the lithiation mechanism for oxygen-terminated Mo_2TiC_2, with the MXene sheets shown in blue and the pillars in orange. (b) *Ex situ* O 1s XPS spectra. (c) *Ex situ* ^{29}Si MAS SS-NMR spectra. (d) *Ex situ* Si 2p XPS spectra.

electrochemical performance seen in the pillared Mo_2TiC_2 is a result of the enlarged interlayer spacing, and not due to the lithiation of SiO_2.

Ex situ O 1s XPS analysis was used to investigate the proposed mechanism of reversible Li_2O formation in Mo_2TiC_2 (Fig. 6b). At OCV there is just one broad peak visible, which is centred on 532.0 eV. Peak deconvolution reveals that there are two main components to this peak at 531.7 eV (assigned to the carbonate oxygen from the electrolyte)[59] and 530.6 eV (which matches the Mo–O_x environment present in the powdered Mo_2TiC_2 material in Fig. 4). There is little change in these two peaks upon cycling, with the shifts varying less than 0.2 eV at all states-of-charge. However, the spectrum for the electrode discharged to 0.01 V shows a new peak at 528.6 eV, which matches well with Li_2O.[49] Upon charging to 3 V, this peak disappears, confirming that Li_2O is reversibly formed and removed upon lithiation (discharging) and delithiation (charging) in the pillared material.

Ex situ solid-state NMR (SS-NMR) was then used to study the evolution of the local structure of the H, Li and F environments within the bulk of the pillared MXene upon cycling. ^{1}H NMR showed a broad peak present in the pristine sample, which is assigned to ^{1}H environments in the polyvinylidene fluoride (PVDF) binder (Fig. S10†).[60] After discharge to 0.01 V, new peaks appear at 3 and 4 ppm, which correspond to carbonate environments originating from retained electrolyte solvent molecules in the material.[60] In addition, a new peak at −1.5 ppm is now present, which can clearly be assigned as LiOH based on previous reports.[60] This peak disappears after charging to 3 V, suggesting that, like Li_2O, the formation of LiOH is reversible. This implies that LiOH is a discharge product, rather than a component of the SEI, which would be expected to still be present upon charging. In addition, all extracted electrodes were washed with DMC to remove SEI and electrolyte residues.

Overall, these results support the mechanism proposed by Anasori *et al.* (reactions (1) and (2)),[19] but imply that an additional reaction involving the formation of LiOH, most likely *via* a conversion reaction with terminal –OH groups, may also occur (reaction (3)).

$$Mo_2TiC_2(OH)_2 + 2Li^+ + 2e^- \rightarrow Mo_2TiC_2 + 2LiOH \quad (3)$$

This reaction could explain the second low voltage discharge peak observed in the $dQ\ dV^{-1}$ plots for both the non-pillared and pillared Mo_2TiC_2 (Fig. S7 and S8†). An analogous conversion reaction involving the formation of LiOH has been previously observed on RuO_2.[60] Comparing the stoichiometries of reactions (1) and (2) with reaction (3) suggests that –OH groups may only provide half as much capacity as –O groups.

Ex situ Raman spectroscopy supports the proposed conversion reactions (Fig. S11†), showing a reduction in the intensity of the Mo–O Raman modes at 170 and 270 cm^{-1} after discharging to 0.01 V, suggesting the cleavage of these bonds.[21] It should be noted that some partial re-oxidation is expected, which may explain the continued presence of the 260 cm^{-1} Raman mode. However, LiOH is also known to have a minor Raman mode at 270 cm^{-1},[61,62] and thus, it could be contributing to the 260 cm^{-1} peak. In addition, LiOH has a major Raman mode at 320 cm^{-1}, which could explain the increase in intensity in this region after discharge.[61,62] However, these modes cannot be conclusively assigned due to the overlap with potential MXene peaks. After discharge, a new mode at *ca.* 550 cm^{-1} matches previous reports for Li_2O, supporting the formation of Li_2O as a discharge product.[61,62] Therefore, these results could support the proposed conversion reaction mechanism whereby the –O and –OH surface functional groups of Mo_2TiC_2 MXene react with Li to form Li_2O and LiOH respectively. Crucially, the Raman spectra confirm that the MXene bonding framework between Mo, C and Ti is unchanged upon cycling despite the conversion reactions unlike with transition metal oxides.[53] This should ensure superior reversibility during the lithiation process of Mo-based MXenes compared to the metal oxides, as suggested by our cycling data.

^{7}Li NMR (Fig. S12†) shows a broad asymmetric peak centred at −0.6 ppm. Deconvolution of this peak using a Lorentzian profile shape for the pristine sample reveals two main environments, the largest of which is assigned as pre-intercalated Li as a result of the LiF–HCl etching method used.[16] A minor peak to the right of this, centred around −1.1 ppm, can be assigned as LiF from the etching stage, which is confirmed as present in the structure by ^{19}F NMR and ^{7}Li–^{19}F HETCOR NMR (Fig. S13†).[63] Upon discharge to 0.01 V, the broad peak shifts to a higher chemical shift (centred at −0.1 ppm), with asymmetry now present on the left side of the peak. This reveals the existence of new Li environments, which are likely to be Li_2O and LiOH based on the previously discussed XPS (Fig. 6b) and ^{1}H NMR (Fig. S10†) data and the relative shifts compared to LiF (3–4 ppm higher than the LiF component).[64] However, the broad profile of the signal, resulting from the slightly disordered nature of MXenes and the lack of separation between the ^{7}Li chemical shift of the different environments,[63,64] means that the environments cannot be unambiguously distinguished in the broad spectra obtained using ^{7}Li NMR. Nevertheless, the ^{7}Li NMR spectra appear to support the XPS and ^{1}H NMR results, confirming the contribution of conversion reactions to the charge storage mechanism. After charging, these changes are reversed, which demonstrates the reversible (de)lithiation of the Mo_2TiC_2 MXene.

Cyclic voltammetry (CV) was used to investigate the reactions and kinetics of the system in more detail. Fig. S14† shows the cyclic voltammograms for five cycles collected at a scan rate of 0.2 mV s^{-1} between 0.01–3 V *vs.* Li^+/Li. Both the non-pillared and pillared MXenes display similar CV features, with small cathodic redox peaks observed at 1.7 and 1.3 V and a large peak below 0.6 V. Above 0.6 V, the voltammograms are fairly rectangular for both materials, indicative of a capacitive-like contribution to the charge storage in this voltage range. On the first cycle, some additional cathodic peaks are observed on discharge at 1.75 and 0.7 V, while the feature below 0.6 V is also more pronounced than on subsequent cycles. These match the extra features observed in the load curves on the first discharge, and are ascribed to irreversible reactions such as SEI formation and Li trapping.[13,50] This helps explain the large initial irreversible capacity loss present in the load curves on the first cycle (Fig. 5).[13,50] After the first cycle, the shape of the CV plots do not notably change, apart from a clear decrease in the current below 0.6 V for the non-pillared material, demonstrating the greater fade observed in this material compared to the pillared MXene, which agrees well with the galvanostatic charge–discharge tests (Fig. 5). The large peak below 0.6 V on discharge and the peak at 1.3 V on charge also match well with the plateaus observed on the load curves (Fig. 5) and $dQ\ dV^{-1}$ plots (Fig. S8†), and with previous reports on Mo_2TiC_2.[19]

To investigate the kinetics of the system in more detail, the cells were then cycled at increasing scan rates of 0.5, 2 and 5 mV s^{-1} (Fig. S15†). As the scan rate increases, both materials show no major changes, with only broadening and small shifts of their redox peaks to lower voltages, suggesting that the majority of the redox reactions are kinetically favoured. The voltammogram run at 5 mV s^{-1} is much more rectangular in shape for Mo_2TiC_2–Si-400 compared to the non-pillared Mo_2TiC_2, with increased current above 1 V. This is indicative of a greater contribution from capacitive charge storage as a result of the higher interlayer spacing and surface area in the pillared MXene, and explains the enhanced high-rate performance of this material.

This is further supported by analysing the proportion of diffusion-limited (battery-like) and surface-limited (capacitive-like) processes to the overall current. It is well known that the relationship between current and scan rate is proportional to the power half when current is diffusion-limited, whereas the relationship is linear (power of 1) when current is surface-limited.[65] This allows the formation of a simple power law to determine the proportion of current arising from diffusion or surface limited processes in a mixed mechanism system, as shown by eqn (4), where i is current, ν is scan rate and a and b are fitting parameters.[65] Plotting the log of the current against the log of the scan rate gives a straight line with a gradient of b, allowing the proportion of diffusion ($b = 0.5$) or surface ($b = 1$) limited current to be quantified.

$$i = a\nu^b \tag{4}$$

When this analysis is carried out at different voltages, the relative contribution of these processes can be studied across the voltage window on the charge and discharge sweeps (Fig. S15c and d†). For both materials, the b-values are closer to 1 (capacitive current) at higher voltages and to 0.5 (diffusion-limited battery-like processes) at low voltages (below 0.6 V). This is expected from the CV shapes, which are more rectangular at higher voltages, with prominent redox peaks present at voltages below 0.6 V. At higher voltages, the pillared Mo_2TiC_2 has a higher b-value (*i.e.* 0.86) than the non-pillared MXene

(0.6–0.8) indicting an increased capacitive contribution to the charge storage resulting from the larger surface area, as previously discussed. In contrast, at low voltages, for example, 0.01 V, the pillared Mo_2TiC_2 has a lower *b*-value (0.56) than the non-pillared Mo_2TiC_2 (0.68), which indicates a greater contribution from battery-like processes at these voltages. This suggests that pillaring leads to increased charge storage contribution from the Li_2O conversion reaction, which explains the substantial increases in capacity compared to the non-pillared MXene.

Electrochemical performance in a sodium-ion battery

Following the promising performance of the Mo_2TiC_2 MXene in a Li-ion system, the non-pillared and pillared materials were further tested as electrodes in Na half-cells. Mo_2TiC_2 has so far not been reported as an electrode for Na-ion batteries. It can be seen that pillaring substantially improves the electrochemical performance, with a 2nd cycle discharge capacity of 109 mA h g^{-1} compared to 74 mA h g^{-1} for the non-pillared material (Fig. 7). By the 80th cycle, the non-pillared MXene had retained a capacity of just 48 mA h g^{-1} (65% capacity retention compared to the 2nd cycle) compared to 82 mA h g^{-1} for the pillared MXene (75% capacity retention). These capacities are much lower than what was observed for the Li-ion system and correspond to a discharge product of approximately $Mo_2TiC_2O_2Na$ (theoretical capacity = 90 mA h g^{-1}), suggesting insertion of one mole of Na per formula unit, even in the pillared MXene. Unlike in the Li-ion system, differential $dQ\,dV^{-1}$ plots show no peaks associated with a conversion reaction for either the pillared or non-pillared Mo_2TiC_2 (Fig. S16†). This suggests that Na_2O does not form, which is in agreement with the DFT studies of Anasori *et al.*[19] At higher rates (Fig. 7d), the pillared MXene has superior capacities compared to the non-pillared material at each rate studied, retaining 40 mA h g^{-1} at 1 A g^{-1}, compared to 16 mA h g^{-1} for the non-pillared MXene.

These findings explain the differences in the behaviour of Mo_2TiC_2 in the Li and Na-ion battery systems. In the Li-ion system, at low voltages the conversion reaction to Li_2O provides a large amount of extra capacity. In contrast, no such conversion reaction occurs in the Na-ion system, which leads to improved cycling stability (in the non-pillared materials), but with capacities around a third of the Li-ion system, even when pillared. CV analysis at different rates reveals that a much greater proportion of the current is surface controlled (capacitive) compared to the Li-ion system (Fig. S17†), for example Mo_2TiC_2–Si-400 has a *b*-value of 0.73 at 0.01 V in the Na-ion system, but 0.56 in the Li-ion system at the same voltage. In the Na system, at voltages above 1 V, the *b*-value for the pillared material is around 0.9, showing that capacitive contributions dominate at higher voltages. This leads to reasonable rate capability (Fig. 7d), with over 40 mA h g^{-1} being retained even at the high rate of 1 A g^{-1}, which is higher than any other report for Mo-based MXenes in Na-ion systems (Table S3†).

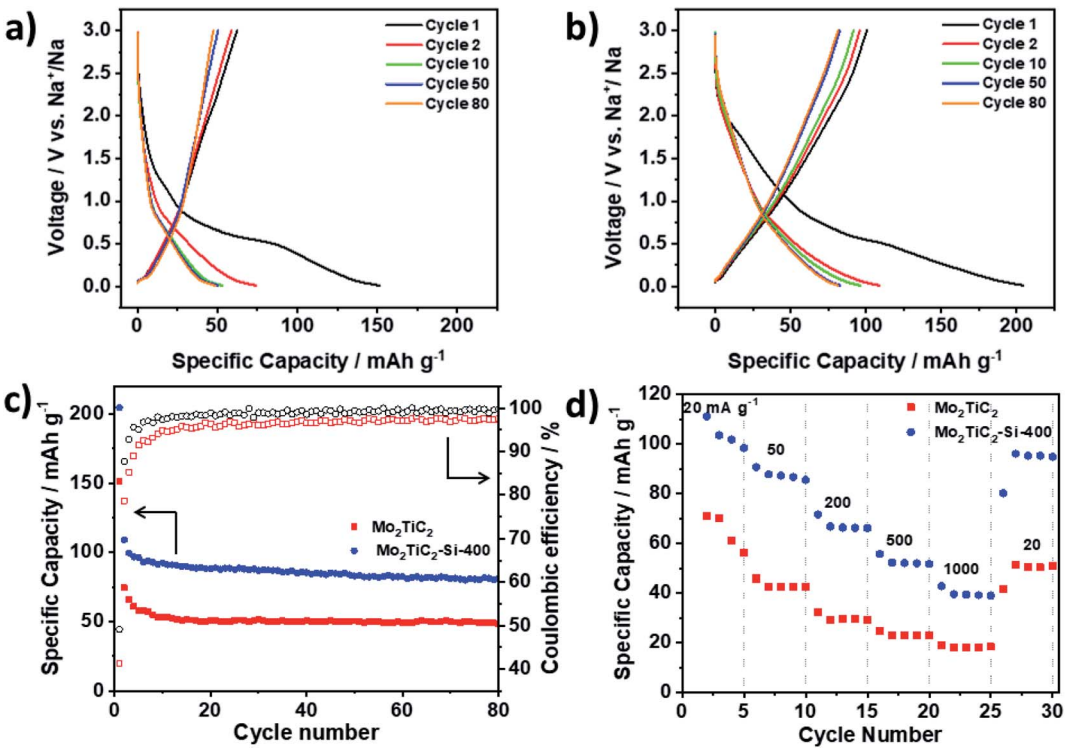

Fig. 7 Galvanostatic discharge–charge load curves of Mo_2TiC_2 samples in Na-ion half-cells in the potential range of 0.01–3 V *vs.* Na^+/Na. (a) Load curves at 20 mA g^{-1} for selected cycles of Mo_2TiC_2. (b) Load curves at 20 mA g^{-1} for selected cycles of Mo_2TiC_2–Si-400. (c) Cycling stability data and coulombic efficiencies over 80 cycles for the pillared (Mo_2TiC_2–Si-400, blue) and non-pillared (Mo_2TiC_2–Si-400, red) samples at 20 mA g^{-1}. (d) Rate capability tests for the pillared (Mo_2TiC_2–Si-400, blue) and non-pillared (Mo_2TiC_2–Si-400, red) samples at increasing rates of 20, 50, 200, 500 and 1000 mA g^{-1} for five cycles each.

Conclusions

Overall, we demonstrate the application of an amine-assisted pillaring method to create porous Mo_2TiC_2. This leads to a large increase in interlayer spacing, achieving *d*-spacings up to 4.2 nm. This corresponds to a gallery height (pore size between layers) of around 3 nm before calcination, which is by far the largest for a Mo-based MXene, and larger than any reports found for other Mo-based layered materials such as MoS_2. This suggests that the amine-assisted silica pillaring method could be applied to a wide range of MXenes, and perhaps other layered materials, if sufficient –OH groups are present on the surface to bind to the amine. Calcination removes the DDA template and reduces the gallery height to a still expanded 1 nm in the final pillared material.

When tested as the negative electrode in a lithium-ion battery, the pillared material showed significantly improved electrochemical performance with respect to the non-pillared material, reaching capacities of up to 316 mA h g^{-1} (89% of the reported theoretical capacity, *i.e.* 356 mA h g^{-1}) based on two moles of Li^+ ions intercalating per formula unit followed by two further moles of Li^+ ions undergoing a conversion reaction. This is the highest capacity reported so far for Mo_2TiC_2. The partially reversible formation of Li_2O during cycling was confirmed by *ex situ* NMR and XPS studies, while *ex situ* NMR suggests that SiO_2 does not undergo redox activity during cycling. Therefore, the enhanced electrochemical performance may be ascribed to the enlarged interlayer spacing. Pillaring increases the capacity and cycling stability of the MXene by providing free space for the formation of Li_2O and intercalation of extra Li ions without allowing layers to restack. In addition, the rate capability is also significantly enhanced, since the enlarged interlayer spacing aids the Li^+ diffusion to the MXene active site. The pillared material shows high coulombic efficiency (*ca.* 100%) and good stability even at a high rate of 1 A g^{-1} (under 8 min charge time) returning 80% of the initial capacity (135 mA h g^{-1}) after 500 cycles. These findings are crucial for the development of other MXenes which are proposed to undergo conversion reactions during lithiation such as V, Ta and Cr chemistries.[66] A potential parallel conversion reaction forming LiOH from –OH surface groups was implied by *ex situ* ^1H NMR and Raman results, but requires further detailed mechanistic studies to confirm the origin of any LiOH formed.

In a Na-ion system, the capacities of the non-pillared and pillared Mo_2TiC_2 MXene were up to a third lower than for the Li-ion system, which could be explained by the charge storage relying on Na^+ intercalation and capacitance, with no conversion reaction occurring. Nevertheless, the pillared material had superior performance compared to the non-pillared MXene, delivering reversible capacities up to 109 mA h g^{-1} at 20 mA g^{-1} over twice that of the non-pillared MXene.

Experimental methods

Materials synthesis and pillaring

For the synthesis of Mo_2TiAlC_2, Mo (−325 mesh, 98% purity, Sigma Aldrich), Ti (−325 mesh, 99% purity, Alfa Aesar), Al (−100 + 325 mesh, 99.5% purity, Alfa Aesar), and C (graphite, <20 μm, 99% purity, Sigma Aldrich) powders were mixed with a pestle and mortar in a 2 : 1 : 1.1 : 2 molar ratio. The mixture was then heated in a tube furnace under flowing argon at 1600 °C for 4 h, with a heating rate of 5 °C min^{-1}. The resulting block was then crushed with a pestle and mortar and ground to give a fine grey powder.

Typically, 3 g of Mo_2TiAlC_2 were slowly added to 30 ml of 9 M HCl with 3 g of pre-dissolved LiF. The mixture was heated to 60 °C and stirred for 5 days. The powder was recovered by centrifuging cycles, with DI water added after each cycle until the pH ≈ 6. The sample was then analysed by PXRD, which showed that significant amounts of unetched MAX phase remained in the sample. Therefore, the partially etched sample was re-dispersed in a fresh etching solution using the same volumes and concentrations used previously. After four days, the solid was collected *via* centrifuging, using the same protocol as described above. A washing step, where the powder was dispersed in 1 M HCl for 3 h at ambient temperature, was used to remove any salt impurities resulting from the etching step. A NaOH washing step was also attempted, but this caused the dissolution of the majority of the powder in approximately 30 min, showing that the Mo_2TiC_2 material is not stable in alkali conditions, in contrast to Ti_3C_2. Leaving the MAX phase to etch for nine consecutive days with no replenishing of the etching solution does not provide a well etched material, even when 12 M HCl is used with 6 g of LiF (the total amount used when the solution is replenished).

400 mg of the etched MXene was then added to a mixture of dodecylamine (DDA) dissolved in TEOS under argon (1 : 10 : 20 MXene : DDA : TEOS molar ratio). This was stirred in a glass vial sealed under argon at ambient temperature for 4 h. The product was then recovered by vacuum filtration and dried on filter paper under vacuum before being re-dispersed in DI water at ambient temperature for 18 h. The intercalated hydrolysis product was then recovered by vacuum filtration and dried overnight at 60 °C, before calcination at 400 °C for 2 h with a heating rate of 5 °C min^{-1} under flowing argon (due to the reactivity of Mo_2TiC_2 with air, Fig. S18†) to give the final pillared Mo_2TiC_2.

Material characterisation

Powder X-ray diffraction (PXRD) was carried out in a Smartlab diffractometer with a 9 kW rotating anode (Rigaku, Tokyo, Japan) using Cu Kα radiation (wavelength of 1.54051 Å) operating in reflection mode with Bragg–Brentano geometry. Prior to PXRD characterisation, all samples were dried in a heated oven at 80 °C for 18 h. The powders were then ground and placed on a glass sample holder and pressed flat with a glass slide.

Scanning electron microscopy (SEM) was performed in a JEOL JSM-7800F (JEOL, Tokyo, Japan), and energy-dispersive X-ray spectroscopy (EDS) was carried out using an X-Max50 (Oxford Instruments, Abingdon, UK) with an accelerating voltage of 10 kV and a working distance of 10 mm. The dried powder samples were dry cast onto a carbon tape support, which was placed on to a copper stub for analysis.

High-angle annular dark-field scanning transmission electron microscopy (HAADF-STEM) was performed in an FEI Titan G2 80–200 'ChemiSTEM' operated at 200 kV at room temperature. STEM-EDS data was acquired with the Titan's Super-X detector system. Hyperspy was used to process all STEM-EDS data, and quantification was performed using the Cliff–Lorimer method with standardless *k*-factors. Each specimen was crushed using a mortar and pestle, dispersed in methanol, drop-cast onto holey carbon-coated copper grids, and dried in a vacuum system ($\sim 10^{-5}$ mbar) at 100 °C for 2 h. STEM cross-sectional imaging was used to measure 100 individual interlayer spacings for each sample for the interlayer distance calculations.

Gas sorption isotherms were measured on a Micromeritics 3 Flex 3500 gas sorption analyser using high purity nitrogen gas at 77 K. BET surface areas were calculated over a relative pressure range of 0.05–0.15P/P_0. Pore size distribution analysis was calculated using the NLDFT (non-linear density functional theory) method with a slit pore model using 3Flex Micromeritics software.

Raman spectroscopy was carried out on a Horiba Lab Raman Spectrometer (Horiba, Minami-ku Kyoto, Japan) with an EM-cooled Synapse camera. Spectra were collected using a 100×, 0.90NA microscope objective. For each measurement, three scans were collected, with a total measurement time of 30 min. The dried powder was sandwiched between two glass microscope slides which were pressed together to give flat MXene particles. One of these slides was then discarded, with the other slide placed flat under the diode green laser (532 nm, 200 μW, 1% intensity) for measurements. For *ex situ* measurements, the extracted discharged electrodes were washed with dimethyl carbonate (DMC), dried in the anti-chamber of an argon-filled glovebox, and transported to the spectrometer in a sealed container. The spectra were collected under air.

Electrochemical characterisation

Pillared and non-pillared Mo_2TiC_2 were tested in coin cells (CR2032 type) in a half-cell configuration using lithium or sodium metal (Tob Energy, China) disks as the counter and reference electrodes and 1 M $LiPF_6$ or $NaPF_6$ in EC/DEC (1 : 1 weight ratio, 99% purity, Gotion) as the electrolyte. The MXene (active material) was mixed with carbon black (super P) as a conductive additive and PVDF as the binder in a 75 : 15 : 10 weight ratio respectively. The mixture was added to a few ml of *N*-methyl-2-pyrrolidone (NMP, 99.5% purity, Alfa Aesar) to make a slurry, which was then cast onto a Cu foil used as current collector, from which electrodes with a diameter of 16 mm were punched. The active mass loading of each electrode was *ca.* 3.2 mg cm^{-2}. Coin cells were constructed in an argon-filled glovebox (O_2 and H_2O levels <0.1 ppm) using Whatman micro glass fibre paper as the separator. Galvanostatic tests were carried out on a Neware battery cycler (Neware Technology Ltd, China) at a current density of 20 mA g^{-1} in the potential range of 0.01–3 V *vs.* Li^+/Li for 94 cycles for the tests in the Li-ion half-cells and in the potential range of 0.01–3 V *vs.* Na^+/Na for 80 cycles for the tests in the Na-ion half-cells. For rate capability tests, the cells were cycled at a current density of 20 mA g^{-1} for 1 cycle to stabilise the cell before 5 cycles were run at each current density of 20, 50, 200, 500 and 1000 mA g^{-1} before returning to 20 mA g^{-1}. For the long-term high-rate cycling test on the pillared MXene, 500 cycles were run at a rate of 1 A g^{-1} after the rate capability test. Cyclic voltammetry (CV) measurements were conducted using an Ivium potentiostat (Ivium Technologies BV, The Netherlands) with increasing scan rates of 0.2, 0.5, 2 and 5 mV s^{-1} for 2 cycles at each rate in the potential range of 0.01–3 V *vs.* Li^+/Li and Na^+/Na for the tests in Li-ion and Na-ion half-cells, respectively. In each case, the final cycle at each scan rate was used to calculate the *b*-values.

***Ex situ* X-ray photoelectron spectroscopy (XPS).** Electrodes were extracted from the cells at different states of charge (*i.e.* OCV, 0.01 V and 3 V). These were washed with dimethyl carbonate (DMC), dried under vacuum in the antechamber of an argon-filled glovebox and sealed under argon in a vial prior to measurement. Samples were analysed using a micro-focused monochromatic Al X-ray source (19.2 W) over an area of approximately 100 μm on a Thermo Fisher Scientific NEXSA spectrometer. Data were recorded at pass energies of 150 eV for survey scans and 40 eV for high-resolution scans with 1 eV and 0.1 eV step sizes respectively. Charge neutralisation of the sample was achieved using a combination of both low energy electrons and argon ions. To remove any surface contaminants, cluster cleaning was performed with 2 keV energy at 0.5 × 0.5 mm area for 60 s. Peak fitting and analysis was carried out using CASA-XPS software.

***Ex situ* solid-state nuclear magnetic resonance spectroscopy (NMR).** ^{19}F, ^{7}Li, ^{1}H and ^{29}Si solid-state NMR spectra were obtained at 16.4 T on a Bruker Advance 700 MHz spectrometer (Bruker Biospin Corporation) operating at Larmor frequencies of 658.6, 272.1, 700.1 and 139.1 MHz, respectively. Spectra were referenced to PTFE ($CF_2 = -122$ ppm), alanine ($NH_3 = 8.5$ ppm) and kaolinite (−91.2 ppm) for ^{19}F, ^{1}H and ^{29}Si, respectively. A 2D ^{19}F–^{7}Li heteronuclear correlation spectrum was obtained using a cross-polarisation based sequence with the contact pulse ramped for ^{19}F. This spectrum was used as an internal reference for the ^{7}Li spectra, (LiF = −1 ppm). Powdered samples were packed, in a nitrogen filled glovebox, into 2.5 mm MAS rotors, and rotated at MAS rates of 15–30 kHz. Pellet electrodes consisting of MXene powders, conductive carbon and PVDF binder in a 75 : 15 : 10 weight ratio were prepared by first mixing the components with a mortar and pestle and then adding small amounts of ethanol as the solvent. Around 25 mg of MXene powder were used in each pellet electrode. These electrodes were then cycled to different states-of-charge (*i.e.* discharged to 0.01 V and charged to 3 V) and then washed with DMC and dried under vacuum in the antechamber of a nitrogen filled glovebox. A pristine electrode was prepared to use as reference.

Conflicts of interest

There are no conflicts to declare.

Acknowledgements

PAM and SS gratefully acknowledge support from the EPSRC Graphene NOWNANO Centre for Doctoral Training for

provision of PhD studentships. NTR is indebted to the Royal Society (RG170150), Energy Lancaster and Lancaster University for financial support. XPS data collection was performed at the EPSRC National Facility for XPS ("HarwellXPS"), operated by Cardiff University and UCL, under contract No. PR16195. Lancaster University NMR facilities were part funded by the European Regional Development Fund (ERDF) under the Collaborative Technology Access Program (cTAP). SJH and SS acknowledge funding from EPSRC (EP/P009050/1) and from the European Research Council Horizon 2020 Starter Grant EvoluTEM (715502). This work was supported by the Henry Royce Institute for Advanced Materials, funded through EPSRC grants EP/R00661X/1, EP/S019367/1, EP/P025021/1 and EP/P025498/1. The authors would like to thank Dr John M Griffin for helpful comments on the manuscript.

References

1 T. Kim, W. Song, D.-Y. Son, L. K. Ono and Y. Qi, Lithium-ion batteries: outlook on present, future, and hybridized technologies, *J. Mater. Chem. A*, 2019, **7**, 2942–2964.
2 M. Li, J. Lu, Z. Chen and K. Amine, 30 Years of Lithium-Ion Batteries, *Adv. Mater.*, 2018, **30**, 1800561.
3 K. J. Griffith, A. C. Forse, J. M. Griffin and C. P. Grey, High-Rate Intercalation without Nanostructuring in Metastable Nb $_2$ O $_5$ Bronze Phases, *J. Am. Chem. Soc.*, 2016, **138**, 8888–8899.
4 C. P. Sandhya, B. John and C. Gouri, Lithium titanate as anode material for lithium-ion cells: a review, *Ionics*, 2014, **20**, 601–620.
5 L. Yan, *et al.*, Recent advances in nanostructured Nb-based oxides for electrochemical energy storage, *Nanoscale*, 2016, **8**, 8443–8465.
6 R. Raccichini, A. Varzi, S. Passerini and B. Scrosati, The role of graphene for electrochemical energy storage, *Nat. Mater.*, 2014, **14**, 271–279.
7 L. Shi and T. Zhao, Recent advances in inorganic 2D materials and their applications in lithium and sodium batteries, *J. Mater. Chem. A*, 2017, **5**, 3735–3758.
8 M. Naguib, *et al.*, Two-dimensional nanocrystals produced by exfoliation of Ti3 AlC2, *Adv. Mater.*, 2011, **23**, 4248–4253.
9 M. Naguib, *et al.*, Two-dimensional transition metal carbides, *ACS Nano*, 2012, **6**, 1322–1331.
10 J.-C. Lei, X. Zhang and Z. Zhou, Recent advances in MXene: Preparation, properties, and applications, *Front. Phys.*, 2015, **10**, 276–286.
11 B. Anasori, M. R. Lukatskaya and Y. Gogotsi, 2D metal carbides and nitrides (MXenes) for energy storage, *Nat. Rev. Mater.*, 2017, **2**, 16098.
12 B. Anasori, M. R. Lukatskaya and Y. Gogotsi, 2D metal carbides and nitrides (MXenes) for energy storage, *Nat. Rev. Mater.*, 2017, **2**, 16098.
13 M. Greaves, S. Barg and M. A. Bissett, MXene-Based Anodes for Metal-Ion Batteries, *Batteries Supercaps*, 2020, **3**, 214–235.
14 C. (John) Zhang, *et al.*, Two-Dimensional Transition Metal Carbides and Nitrides (MXenes): Synthesis, Properties, and Electrochemical Energy Storage Applications, *Energy Environ. Mater.*, 2020, **3**, 29–55.
15 F. Bu, *et al.*, Porous MXenes: Synthesis, structures, and applications, *Nano Today*, 2020, **30**, 100803.
16 R. Garg, A. Agarwal and M. Agarwal, A review on MXene for energy storage application: effect of interlayer distance, *Mater. Res. Express*, 2020, **7**, 022001.
17 L. Verger, V. Natu, M. Carey and M. W. Barsoum, MXenes: An Introduction of Their Synthesis, Select Properties, and Applications, *Trends Chem.*, 2019, **1**, 656–669.
18 J. Pang, *et al.*, Applications of 2D MXenes in energy conversion and storage systems, *Chem. Soc. Rev.*, 2019, **48**, 72–133.
19 B. Anasori, *et al.*, Two-Dimensional, Ordered, Double Transition Metals Carbides (MXenes), *ACS Nano*, 2015, **9**, 9507–9516.
20 J. Zhang, *et al.*, Single platinum atoms immobilized on an MXene as an efficient catalyst for the hydrogen evolution reaction, *Nat. Catal.*, 2018, **1**, 985–992.
21 C. Chen, *et al.*, MoS_2-on-MXene Heterostructures as Highly Reversible Anode Materials for Lithium-Ion Batteries, *Angew. Chem., Int. Ed.*, 2018, **57**, 1846–1850.
22 H. Kim, B. Anasori, Y. Gogotsi and H. N. Alshareef, Thermoelectric Properties of Two-Dimensional Molybdenum-Based MXenes, *Chem. Mater.*, 2017, **29**, 6472–6479.
23 Y. Gao, *et al.*, Mo_2TiC_2 MXene: A Promising Catalyst for Electrocatalytic Ammonia Synthesis, *Catal. Today*, 2020, **339**, 120–126.
24 K. Cao, T. Jin, L. Yang and L. Jiao, Recent progress in conversion reaction metal oxide anodes for Li-ion batteries, *Mater. Chem. Front.*, 2017, **1**, 2213–2242.
25 J. T. Kloprogge, Synthesis of Smectites and Porous Pillared Clay Catalysts: A Review, *J. Porous Mater.*, 1998, **5**, 5–41.
26 J. Luo, *et al.*, Sn(4+) Ion Decorated Highly Conductive Ti3C2 MXene: Promising Lithium-Ion Anodes with Enhanced Volumetric Capacity and Cyclic Performance, *ACS Nano*, 2016, **10**, 2491–2499.
27 J. Luo, *et al.*, Pillared Structure Design of MXene with Ultralarge Interlayer Spacing for High-Performance Lithium-Ion Capacitors, *ACS Nano*, 2017, **11**, 2459–2469.
28 J. Luo, *et al.*, Tunable pseudocapacitance storage of MXene by cation pillaring for high performance sodium-ion capacitors, *J. Mater. Chem. A*, 2018, **6**, 7794–7806.
29 J. Luo, *et al.*, Pillared MXene with Ultralarge Interlayer Spacing as a Stable Matrix for High Performance Sodium Metal Anodes, *Adv. Funct. Mater.*, 2019, **29**, 1805946.
30 S. Sun, Z. Xie, Y. Yan and S. Wu, Hybrid energy storage mechanisms for sulfur-decorated Ti3C2 MXene anode material for high-rate and long-life sodium-ion batteries, *Chem. Eng. J.*, 2019, **366**, 460–467.
31 Y. Tian, *et al.*, Surface nitrogen-modified 2D titanium carbide (MXene) with high energy density for aqueous supercapacitor applications, *J. Mater. Chem. A*, 2019, **7**, 5416–5425.
32 Y. Li, *et al.*, Tunable energy storage capacity of two-dimensional $Ti_3C2T:X$ modified by a facile two-step pillaring strategy for high performance supercapacitor electrodes, *Nanoscale*, 2019, **11**, 21981–21989.

33 P. A. Maughan, N. Tapia-Ruiz and N. Bimbo, In-situ pillared MXene as a viable zinc-ion hybrid capacitor, *Electrochim. Acta*, 2020, **341**, 136061.
34 B. Anasori, *et al.*, Mo_2TiAlC_2: A new ordered layered ternary carbide, *Scr. Mater.*, 2015, **101**, 5–7.
35 M. Ghidiu, M. R. Lukatskaya, M.-Q. Zhao, Y. Gogotsi and M. W. Barsoum, Conductive two-dimensional titanium carbide 'clay' with high volumetric capacitance, *Nature*, 2014, **516**, 78–81.
36 J. Halim, *et al.*, Synthesis and Characterization of 2D Molybdenum Carbide (MXene), *Adv. Funct. Mater.*, 2016, **26**, 3118–3127.
37 P. A. Maughan, *et al.*, Porous Silica-Pillared MXenes with Controllable Interlayer Distances for Long-Life Na-Ion Batteries, *Langmuir*, 2020, **36**, 4370–4382.
38 R. Meshkian, *et al.*, Synthesis of two-dimensional molybdenum carbide, Mo2C, from the gallium based atomic laminate Mo_2Ga_2C, *Scr. Mater.*, 2015, **108**, 147–150.
39 A. Byeon, *et al.*, Two-Dimensional Titanium Carbide MXene As a Cathode Material for Hybrid Magnesium/Lithium-Ion Batteries, *ACS Appl. Mater. Interfaces*, 2016, **9**(5), 4296–4300.
40 S.-M. Paek, H. Jung, M. Park, J.-K. Lee and J.-H. Choy, An Inorganic Nanohybrid with High Specific Surface Area: TiO 2 -Pillared MoS 2, *Chem. Mater.*, 2005, **17**, 3492–3498.
41 X. Xie, *et al.*, Porous $Ti_3C_2T_x$ MXene for Ultrahigh-Rate Sodium-Ion Storage with Long Cycle Life, *ACS Appl. Nano Mater.*, 2018, **1**, 505–511.
42 W. Bao, *et al.*, Porous Cryo-Dried MXene for Efficient Capacitive Deionization, *Joule*, 2018, **2**, 778–787.
43 C. E. Ren, *et al.*, Porous Two-Dimensional Transition Metal Carbide (MXene) Flakes for High-Performance Li-Ion Storage, *ChemElectroChem*, 2016, 689–693, DOI: 10.1002/celc.201600059.
44 Y. Wang, *et al.*, Three-dimensional porous MXene/layered double hydroxide composite for high performance supercapacitors, *J. Power Sources*, 2016, **327**, 221–228.
45 S. Gong, G. Zhao, P. Lyu and K. Sun, A Pseudolayered MoS_2 as Li-Ion Intercalation Host with Enhanced Rate Capability and Durability, *Small*, 2018, **14**, 1803344.
46 A. Djire, *et al.*, Pseudocapacitive Storage in Nanolayered Ti2NTx MXene Using Mg-Ion Electrolyte, *ACS Appl. Nano Mater.*, 2019, **2**, 2785–2795.
47 C. J. Zhang, *et al.*, Oxidation Stability of Colloidal Two-Dimensional Titanium Carbides (MXenes), *Chem. Mater.*, 2017, **29**, 4848–4856.
48 W. Liu, *et al.*, Investigation of zinc ion storage of transition metal oxides, sulfides, and borides in zinc ion battery systems, *Chem. Commun.*, 2017, **53**, 6872–6874.
49 C. Nita, *et al.*, Eco-friendly synthesis of SiO2 nanoparticles confined in hard carbon: A promising material with unexpected mechanism for Li-ion batteries, *Carbon*, 2019, **143**, 598–609.
50 X. Tang, X. Guo, W. Wu and G. Wang, 2D Metal Carbides and Nitrides (MXenes) as High-Performance Electrode Materials for Lithium-Based Batteries, *Adv. Energy Mater.*, 2018, **8**, 1801897.
51 J. Mei, G. A. Ayoko, C. Hu, J. M. Bell and Z. Sun, Two-dimensional fluorine-free mesoporous Mo2C MXene *via* UV-induced selective etching of Mo2Ga2C for energy storage, *Sustainable Mater. Technol.*, 2020, **25**, e00156.
52 M. Naguib, *et al.*, MXene: a promising transition metal carbide anode for lithium-ion batteries, *Electrochem. Commun.*, 2012, **16**, 61–64.
53 K. Cao, T. Jin, L. Yang and L. Jiao, Recent progress in conversion reaction metal oxide anodes for Li-ion batteries, *Mater. Chem. Front.*, 2017, **1**, 2213–2242.
54 J. H. Ku, J. H. Ryu, S. H. Kim, O. H. Han and S. M. Oh, Reversible Lithium Storage with High Mobility at Structural Defects in Amorphous Molybdenum Dioxide Electrode, *Adv. Funct. Mater.*, 2012, **22**, 3658–3664.
55 D. Wu, *et al.*, Mixed Molybdenum Oxides with Superior Performances as an Advanced Anode Material for Lithium-Ion Batteries, *Sci. Rep.*, 2017, **7**, 1–9.
56 K. Tang, S. A. Farooqi, X. Wang and C. Yan, Recent Progress on Molybdenum Oxides for Rechargeable Batteries, *ChemSusChem*, 2019, **12**, 755–771.
57 A. I. Freytag, A. D. Pauric, M. Jiang and G. R. Goward, ^{7}Li and ^{29}Si NMR Enabled by High-Density Cellulose-Based Electrodes in the Lithiation Process in Silicon and Silicon Monoxide Anodes, *J. Phys. Chem. C*, 2019, **123**, 11362–11368.
58 B. Key, *et al.*, Real-time NMR investigations of structural changes in silicon electrodes for lithium-ion batteries, *J. Am. Chem. Soc.*, 2009, **131**, 9239–9249.
59 R. Dedryvère, *et al.*, *XPS Identification of the Organic and Inorganic Components of the Electrode/Electrolyte Interface Formed on a Metallic Cathode*, 2019, DOI: 10.1149/1.1861994.
60 Y. Y. Hu, *et al.*, Origin of additional capacities in metal oxide lithium-ion battery electrodes, *Nat. Mater.*, 2013, **12**, 1130–1136.
61 A. C. Stowe and N. Smyrl, Raman spectroscopy of lithium hydride corrosion: Selection of appropriate excitation wavelength to minimize fluorescence, *Vib. Spectrosc.*, 2012, **60**, 133–136.
62 A. Sifuentes, A. C. Stowe and N. Smyrl, Determination of the role of Li2O on the corrosion of lithium hydride, *J. Alloys Compd.*, 2013, **580**, S271–S273.
63 S. Haber and M. Leskes, What Can We Learn from Solid State NMR on the Electrode-Electrolyte Interface?, *Adv. Mater.*, 2018, **30**, 1706496.
64 B. M. Meyer, N. Leifer, S. Sakamoto, S. G. Greenbaum and C. P. Grey, High field multinuclear NMR investigation of the SEI layer in lithium rechargeable batteries, *Electrochem. Solid-State Lett.*, 2005, **8**, A145.
65 V. Augustyn, *et al.*, High-rate electrochemical energy storage through Li+ intercalation pseudocapacitance, *Nat. Mater.*, 2013, **12**, 518–522.
66 Y. Guo, *et al.*, Synthesis of two-dimensional carbide Mo2CTx MXene by hydrothermal etching with fluorides and its thermal stability, *Ceram. Int.*, 2020, **46**, 19550–19556.